2012

Visualization of Vapor Formation Regimes during Capillary-Fed Boiling in Sintered-Powder Heat Pipe Wicks

J. A. Weibel
Purdue University, jaweibel@purdue.edu

S V. Garimella
Purdue University, sureshg@purdue.edu

Weibel, J. A. and Garimella, S V., "Visualization of Vapor Formation Regimes during Capillary-Fed Boiling in Sintered-Powder Heat Pipe Wicks" (2012). *CTRC Research Publications.* Paper 175.
http://dx.doi.org/http://dx.doi.org/10.1016/j.ijheatmasstransfer.2012.03.021

Visualization of Vapor Formation Regimes during Capillary-Fed Boiling in Sintered-Powder Heat Pipe Wicks*

Justin A. Weibel, Suresh V. Garimella†

School of Mechanical Engineering and Birck Nanotechnology Center
Purdue University, 585 Purdue Mall, West Lafayette, IN 47907 USA

Abstract

The current study investigates capillary-fed boiling of water from porous sintered powder wicks used in emerging high-effective-conductivity vapor chamber heat spreaders intended for management of hot spots with heat fluxes exceeding 500 W cm^{-2}. Characterization of 1 mm-thick wicks composed of 100 μm sintered copper particles is performed in a test facility which replicates the capillary feeding conditions that occur in such devices. Boiling curves are obtained for a 5 mm × 5 mm heated input area, along with high-speed *in-situ* visualization of the evaporation/boiling processes. Understanding the vapor formation regimes is essential to predictive modeling of the observed characteristics. Schematic representations of such regimes along the boiling curves are presented for homogeneous and modified wick structures. In general, incipience of boiling in sintered-powder wicks reduces the effective thermal resistance and, for small heat input areas, does not cause liquid starvation due to a capillary limitation. The thermal performance enhancement provided by two different augmentation methods is quantified and explained in terms of the observed vapor formation characteristics. Patterns fabricated within the sintered powder create multi-scale wicks with regions of different pore size. These patterns reduce thermal resistance throughout the boiling regime by increasing the permeability to vapor exiting the wick, as confirmed by visualization of the preferential vapor venting from the surface. At the highest heat fluxes investigated prior to dryout, a thin liquid film is observed to form in the recessed patterned areas at the base of the wick. Integration of copper-coated carbon nanotubes on to the sintered powder reduces the required superheat for boiling incipience, thus reducing the overall thermal resistance at low heat fluxes. Evaporation and boiling regime heat transfer predictions from several available correlations are compared to the current results, and are shown to corroborate the conclusions regarding vapor permeability.

Nomenclature

A_c	heat input area

* Submitted for publication in *International Journal of Heat and Mass Transfer*, February 2012
† Corresponding author: Tel. 1 765 494 5621 ; sureshg@purdue.edu

$\mathrm{A}_{c,p}$	characteristic pore area $(\pi D_p^2/4)$
c_p	specific heat
CC	co-continuous k_{eff} model
D	particle diameter
D_p	pore diameter $(0.42D)$
EMT	effective medium theory k_{eff} model
h_{lg}	latent heat of vaporization
Ja	Jakob number $\left(\rho_l c_{p,l}\Delta T_{sl}/\rho_g h_{\mathrm{lg}}\right)$
k	thermal conductivity
k_{eff}	effective thermal conductivity
K	permeability $(\varepsilon D_p^2/32)$
L_e	characteristic length $[(D_p(\mathrm{A}_{c,p}/\mathrm{P}_p)^4)^{0.2}]$
ME1	Maxwell-Eucken k_{eff} model (continuous Cu phase)
ME2	Maxwell-Eucken k_{eff} model (continuous liquid phase)
P_p	characteristic pore perimeter (πD_p)
q''	heat flux
R	sample thermal resistance
t_s	solder thickness
T	temperature
T_{ref}	vapor reference temperature
T_{sat}	saturation temperature
$T_{substrate}$	substrate temperature
ΔT_{sl}	surface to liquid/vapor saturation temperature drop
ΔT^*	nucleation temperature drop $(4\sigma T_{sat}/\rho_g h_{\mathrm{lg}} D_p)$
U	uncertainty
x	x-coordinate location

Greek symbols

δ	wick layer thickness
ε	porosity
ρ	density

σ	surface tension
μ	dynamic viscosity
υ	kinematic viscosity

Subscripts

boil	boiling regime
Cu	copper
evap	evaporation regime
g	vapor phase
l	liquid phase
s	solder

Keywords: capillary, thin-film evaporation, boiling, visualization, heat pipe, sintered powder wick

1. Introduction

State-of-the-art military and automotive electronics systems with high power densities require the removal of large quantities of heat to maintain adequate performance and ensure device reliability. The objective of emerging cooling technologies is to extend current limitations to accommodate these increasingly high heat flux sources while simultaneously minimizing the junction-to-ambient thermal resistance. A heat pipe or vapor chamber heat sink is ideally suited for such applications that demand reliability and high performance. Such a device consists of a hollow, thermally conductive shell lined with a porous wick material and charged with a working fluid; copper-water systems are typical for electronics cooling. At one end, termed the evaporator, heat is absorbed into the evaporating or boiling working fluid and the generated vapor flows to the condenser side, where it gives up heat to an ultimate heat sink and condenses back to the liquid state. Liquid is continually replenished at the evaporator via the porous lining which pumps liquid from the condenser by means of capillary forces. High effective conductivities of this two-phase operating mechanism are attributable to the latent heat exchange at nearly constant temperature. The lack of moving components or mechanical pumping contributes to their reliable and simple operation. As a result, heat pipes have found widespread use in low-power-dissipation consumer electronics. However, there are several challenges which must be addressed to accommodate higher heat fluxes.

The maximum heat flux input of a heat pipe is commonly limited by operating conditions which result in evaporator dryout. This can be caused by either a lack of capillary driven bulk fluid supplied to the evaporator (known as the capillary limit), or by aggressive boiling in the wick which forms a vapor blanket over the surface and cuts off liquid supply (the boiling limit). In order to extend the range of

utility of heat pipes, novel evaporator materials and designs that avoid such dryout limitations must be demonstrated. Also, to maintain the electronics at acceptable temperatures while dissipating increasingly higher power densities, the overall thermal resistance of the heat pipe must be reduced. The evaporator thermal resistance is the primary individual contributor to the overall value [1]. The focus of the current study is to investigate the vapor formation characteristics of novel evaporator structures that have previously been shown to lower capillary-fed boiling thermal resistance through feasibility models [2] and experiments [3]. The current study provides further insight into the fundamental two-phase mechanisms that govern improved evaporator performance.

Several novel facilities have recently been developed which closely recreate capillary-feeding conditions and examine conventional wick materials. Hanlon and Ma [4] and Davis and Garimella [5] measured low heat flux evaporation heat transfer coefficients from thin sintered powder layers. Weibel *et al.* [6]investigated sintered-powder wicks over a large range of heat fluxes and parametrically characterized wick thermal resistance dependence on wick thickness and powder size. In a series of studies by Li *et al.* [7-9], the effects of wick thickness, porosity, and pore size on the thermal resistance and dryout characteristics of sintered screen mesh wicks were quantified, and visual observation was used to identify evaporation, boiling, and dryout regimes.

One approach to improving conventional heat pipe wick materials and realizing the performance gains discussed above is through the use of patterned or multi-scale wicks which have greatly varying pore sizes within the same evaporator. The rationale for such a wick structure is that the smaller-scale pores extend the capillary limit by generating a large capillary pressure to draw the liquid flow, while the larger-scale pores act as conduits of low flow resistance for the bulk transport of fluid. Additionally, in the evaporator, boiling performance can be improved as larger pores provide high-permeability ventilation paths for the vapor, while the smaller pores continue to supply liquid and act as sites for film evaporation or bubble nucleation. Zhao and Chen [10] investigated capillary-fed evaporation/boiling from sintered copper wicks with 150 – 500 μm grooves and found the dryout heat flux to be extended by 350% compared to uniform sintered powder wicks. Biporous sintered powder wicks composed of large diameter clusters of smaller diameter particles are another example of multi-scale wicks. Semenic and Catton [11] explored the dryout heat flux and thermal resistance dependence on cluster diameter, particle diameter, and biporous wick thickness, while Merilo [12] performed *in situ* visualization of bubble nucleation from similar biporous wicks; both studies cited improved performance compared to conventional sintered powder.

A second augmentation approach is the integration of carbon nanotube (CNT) arrays into conventional heat pipe wick structures on account of their advantageous thermal and mechanical characteristics. The inherent porosity of a CNT array facilitates its use as a capillary liquid pump as

demonstrated by Zhou *et al.* [13], who explored the interstitial flow characteristics of multiple fluids through CNT nanowicks. Ranjan *et al.* [14] numerically investigated the enhancement in evaporative heat transfer due to the addition of CNT nanowicks grown on to conventional copper microwicks, and found that the increased liquid thin-film area in the nanopores of the CNT array resulted in reduced evaporation thermal resistance. In order to fabricate heat pipes with integrated CNT nanowicks for electronics cooling, they must be made compatible with water, the optimal working fluid at the operating temperatures of interest. It is well known that water poorly wets individual CNTs; when formed into densely packed aligned arrays, they exhibit superhydrophobic behavior [16]. Because their capillary pumping ability is heavily influenced by these wetting properties, surface treatments or coatings must be applied to CNTs to improve their hydrophilicity. Uniform metallization of CNT arrays with copper is an ideal solution that rests on the well-established understanding of wettability and long-term compatibility properties of conventional copper-water systems. While multiple techniques have been adopted for coating CNTs with copper [17,18], Powell [19] developed a novel method for uniformly coating CNT arrays via e-beam evaporation. The copper coating was shown to render the surface hydrophilic and also preserved the structural arrangement of the CNT array following wetting of the surface, unlike their uncoated counterparts.

Multiple studies in the literature have observed increased pool boiling heat transfer coefficients and critical heat flux (CHF) through CNT integration and coating of boiling surfaces [20-23]. However, the enhancement was observed for dielectric wetting fluids and water was not investigated. Also, the fundamental mechanisms of heat transfer in pool boiling from a submerged wick sample differ from that with a capillary-fed liquid supply and under the vapor interface conditions of a heat pipe evaporator. Investigation of capillary-fed evaporators incorporating hydrophilic CNTs for performance enhancement has been limited. Hashimoto *et al.* [30] manufactured a working high heat flux vapor chamber and showed that coating a sintered powder evaporator with CNTs reduced the overall device thermal resistance by up to 27% at an input heat flux of 500 W cm^{-2}. A lone example of an evaporator combining both patterning and CNT enhancement was reported by Cai and Chen [31]. A capillary-fed hydrophilic CNT array patterned with 50 μm grooves was shown to support 600 W cm^{-2} at 35-45 °C superheat over a 2 mm x 2 mm heat input area.

The current work builds upon earlier investigations that attempted to combine both CNT and multi-scale augmentation methods to improve heat pipe performance. Several evaporator samples comprised of a copper-metallized CNT array covering the heat input area and surrounded by screen mesh were previously evaluated using the same test facility as in this work [36]. Varying the CNT growth parameters and the resulting array characteristics yielded an optimal recipe for reducing the evaporator thermal resistance. However, a lack of liquid supply to the center of the large CNT array coverage area

limited the performance. A numerical study [2] revealed that extremely low fluid permeability through the nanopores of the CNT array causes dryout and prohibits their use as the sole liquid-carrying medium over large heat input areas. A novel evaporator design was proposed which incorporated micro-patterned sintered powder into the central CNT array; a schematic diagram of this evaporator section design is shown in Figure 1. The analysis demonstrated that the sintered powder helps carry liquid to the CNT areas, preventing dryout. In a subsequent study [3], integrated nanostructured wicking surfaces of this kind were fabricated and tested. Detailed discussion of the CNT fabrication techniques and resulting nanowick morphology, as well as initial estimates of the enhancement provided, were presented.

In an effort to further understand and improve such evaporator structures, evaporation and boiling mechanisms are carefully studied through *in situ* high-speed visualization of the sample surfaces in the current study. These mechanisms are then related to the measured thermal resistance trends. Identification of operating regimes and critical transitions for patterned and nanostuctured evaporators along the boiling curve provide the first step toward developing performance prediction tools. Available predictive methods for the surface superheat under evaporation (based on the saturated wick thermal conductivity) and boiling are briefly reviewed, and predictions compared to the current results.

2. Evaporator sample preparation

All of the wick test surfaces are prepared on individual sample substrates that can be inserted as needed into the test facility. The 0.5 mm thick substrates are composed of laminated copper-molybdenum-copper (13%-74%-13%) sheets which have a thermal expansion coefficient matching that of silicon. A substrate of this material and thickness is chosen because it represents the likely wall composition of an ultrathin vapor chamber heat spreader which can be directly mounted on electronic components. The porous microwick for all test samples is a 1 mm thick layer of 100 μm sintered copper particles having a volumetric open porosity of 50%. The sintering process was performed by Thermacore, Inc. Three variants of microwicks are investigated: a uniform homogeneous wick, a wick with a grid pattern fabricated into the powder, and a wick with a radial pattern of wedges formed into the powder. The dimensions of these three geometries is provided in Figure 2. The patterns are formed in the center of the sample directly over a 5 mm × 5 mm heat input location on the back side of the substrate. While the grid and wedge patterns were heuristically proposed, the chosen length scales of the open pores are informed by a numerical flow analysis optimization [2] that considered practical fabrication method limitations. Also, for all samples, a strip of exposed substrate area lines the outer edge to allow sealing of the sample into the test facility as explained in the next section.

To evaluate the effects of nanostructuring, CNTs are grown over the sintered powder wick. The CNTs for the current study were synthesized in the laboratory of Professor Timothy S. Fisher of Purdue

University at the Birck Nanotechnology Center. A detailed description of the synthesis, functionalization procedure, and resulting nanowick morphology for the samples tested here is available in [3]. The CNT growth is performed in a microwave plasma chemical vapor deposition (MPCVD) chamber using a titanium-aluminum-iron (60-10-3 nm, respectively) tri-layer catalyst. The synthesis process resulted in an array of 10 μm long, 50 nm diameter nanotubes coating the upper layer of sintered powder particles and the exposed substrate areas. In order to render the CNTs hydrophilic, a uniform layer of copper of roughly 10 nm thickness was deposited over the nanotubes via e-beam evaporation. Conversion of the array from hydrophobic to hydrophilic was confirmed by the drastic decrease in the macroscopic contact angle of static droplets placed on the sample surfaces.

In total, five different evaporator samples are fabricated for comparison. A bare (not coated with CNTs) homogeneous sintered powder wick, H:0, serves as the baseline for comparison to all other samples. Two additional bare samples, G:0 and W:0, feature both grid and wedge-patterned sintered powder wicks to provide a means for evaluating and understanding the effects of such surface modifications independent of CNT nanostructuring. Finally, a homogeneous CNT-coated sample (H:1) and a grid-patterned CNT-coated sample (G:1) are tested to observe the enhancement provided by nanostructuring.

3. Experimental facility, test procedures, and data reduction

Measurement of sample thermal performance and *in situ* visualization of the test surfaces are performed in the experimental apparatus described in this section. The principal capability of the facility is that it recreates the saturated environment and capillary liquid feeding conditions present in the evaporator section of a heat pipe or vapor chamber. The facility components and operating procedures are briefly discussed below; additional details are available in [17].

The test chamber, shown in Figure 3 (a), is composed of PEEK and transparent polycarbonate walls with a liquid inlet at the base and liquid outlet on the side wall. An external flow loop circulates water that is heated to the saturation temperature through the chamber, thereby maintaining the vertical level of the internal liquid bath at the outlet height. The outlet is positioned at a height such that the liquid bath level overlaps the lower edge of the porous test sample surface which is sealed vertically against the wall of the test chamber, exposing only the porous wick to the chamber interior. An insulated copper heater block supplies heat to the back of the sample through a 5 mm × 5 mm area in the center of the sample. Supply of liquid to the lower sample edge allows capillary wicking of water to the heat input area located 8.25 mm above. In this way, the test facility reproduces the capillary-feeding mechanism and internal conditions within a heat pipe. All tests in this study are performed at atmospheric pressure.

Two primary measurement systems are operated concurrently during testing – high-speed visualization and thermal measurement. The plan view of the test chamber shown in Figure 3 (b) identifies the various visualization system components. Two translatable borescopes provide views that are normal and at a 45° angle to the sample surface. Flexible polyimide film heaters are attached to the borescope tips in order to eliminate condensation on the lens. A Photron Fastcam-X 1024PCI camera is mounted on the other end of the borescope, while dual 300 W xenon arc lamp sources feed inline light to illuminate the surface during high-speed image capture. The camera/lighting system as implemented provides clear video images of the surface at up to 15,000 frames per second (fps).

The temperature measurement system consists of a linear array of thermocouples embedded into the copper heater block and a vapor reference thermocouple centered above the heated surface (Figure 3 (c)). A linear temperature gradient is measured along the thermocouple array, which allows the heat flux provided to the back of the substrate to be computed. Calculation of the input heat flux by this method effectively accounts for and subtracts all wiring electrical losses and natural convection heat loss through heater block insulation. The substrate temperature is calculated by extrapolating the temperature drop through the solder joint according to

$$T_{substrate} = T_4 - q''\left[\frac{(x_5 - x_4)}{k_{Cu}} + \frac{t_s}{k_s}\right]. \quad (1)$$

From these measurements, a boiling curve is produced by plotting the heat flux *q''* against the substrate superheat temperature. The effective sample thermal resistance, which includes substrate conduction, wick conduction, and evaporation/boiling resistances, is defined as

$$R = \frac{T_{substrate} - T_{ref}}{q'' A_c}. \quad (2)$$

The uncertainty in these calculated quantities is predicted based on several measurement and system uncertainties as follows: U_T, ± 0.3 °C; U_X, ± 0.08 mm; U_{ts}, ± 25%; U_{ks}, ± 5%; and U_{Ac}, ± 1x10^{-4} mm^2.

The surface wetting characteristics of the samples are observed to change dramatically from hydrophilic to hydrophobic if the samples are left exposed to the atmosphere for extended durations due to oxidation of the copper surfaces. Therefore, multiple precautionary steps are taken to minimize oxidation. Following fabrication, all samples are placed in evacuated containers during temporary storage. Prior to testing, each sample is placed in a reducing hydrogen atmosphere to remove any minor copper surface oxidation which may have occurred. The sample substrate is soldered to a copper heater block in a purged inert argon atmosphere, as another measure to limit surface oxidation. A 0.004 in. (~0.102 mm) thick Pb-Sn solder joint is formed by heating the substrate approximately 25 °C above the solder melting point (178 °C).

To begin the test procedure, the liquid in the chamber is vigorously boiled to remove all non-condensable gases through the reflux condenser. Once this purge is complete, the inline heater in the liquid flow loop is set to achieve saturation temperature in the chamber. Each data point on the boiling curve corresponds to a fixed input heat flux at which the heater block temperatures are allowed to stabilize. A steady state is defined as being reached when the time-averaged variation of the substrate temperature over a 10-minute interval is less than 0.1 °C/min. Time-averaged steady-state heater block temperature measurements over a period of 5 mins are used to predict the substrate temperature and sample resistance using Equation (1) and (2). Following collection of steady-state data for processing, the corresponding surface evaporation/boiling characteristics are viewed with the high-speed camera. The visualization must be performed after collection of the temperature data because the lighting required for visualization temporarily increases the vapor reference temperature. This procedure is repeated with increasing heat inputs to develop the entire boiling curve. Smaller heat flux increments are used in the vicinity of critical regime transitions to allow for greater resolution of these events on the boiling curve. The heat flux during testing is continually increased until either a catastrophic dryout-induced temperature overshoot is observed or until the melting point of the heater-to-sample solder joint is reached.

4. Experimental results and discussion

4.1. Thermal characterization and visualization

Test results obtained for the fabricated samples using the experimental methods described above are now presented. For each sample, a boiling curve of the input heat flux versus the substrate superheat as well as a curve of thermal resistance versus input heat flux are developed. The ability of a sample to maintain a lower superheat for a given heat flux (i.e., a shift to the left on the boiling curve) is indicative of superior performance and a lower associated thermal resistance. Additionally, high-speed video of the surfaces was captured for each data point appearing on these plots to identify the concurrent heat transfer mechanism. Several frame-by-frame excerpts from this large catalog of videos are presented as necessary to better illustrate the relationship between the identified mechanisms and trends in the thermal performance data. These videos are available as Supplementary data provided with this paper and available online.

4.1.1. CNT-coated versus uncoated homogeneous sintered powder wicks

The first set of boiling and resistance curves is presented in Figure 4. These plots compare the results for a bare (sample H:0) and a CNT-coated homogeneous (sample H:1) wick, to evaluate the effects of the presence of a CNT array on the sintered powder. The bare homogeneous sintered powder heat pipe wick

serves as a baseline for comparison of all the samples investigated, and therefore it is important to review the fundamental trends in the performance of this sample. The solid-line boiling curve in Figure 4(a) for sample H:0 initially shows a nearly linear increase in substrate superheat temperature with increasing input heat flux until a drastic 4.7° drop is measured at 70.4 W cm^{-2}. Visualization confirms that the sample is fully saturated with liquid for heat fluxes up to the point of this sharp reduction, and heat transfer occurs via evaporation from a static liquid-vapor free interface from the top of the wick layer. The drop in superheat temperature coincides with incipience of boiling at the base of the wick. As explained in [19], the performance gain (temperature drop) can be attributed to the transition in heat transfer mechanism from evaporation at the top of the wick to boiling from the base of the wick. This change in the location of the phase change process effectively eliminates the saturated wick conduction resistance in the heat flow path between the substrate to the vapor space. Once in the boiling regime, there is again a linear dependence of superheat on increasing input heat flux. The steeper slope of the curve in this regime is indicative of a higher heat transfer coefficient than in the evaporation regime. Testing of the sample was stopped at 514 W cm^{-2} because the temperature of the heater-to-substrate solder joint approached the melting temperature of the solder; this limiting heat flux is not indicative of a sample thermal performance limitation. The thermal resistance curve for sample H:0, shown in Figure 4(b), mirrors the trends identified in the boiling curve. At low heat fluxes there is initially a relatively larger thermal resistance until incipience of boiling causes an immediate drop to approximately 0.35 °C/W where it remains relatively constant throughout the boiling regime.

The dashed lines in Figure 4 represent the boiling and thermal resistance curves for the CNT-coated homogeneous sample H:1. The immediately recognizable difference between the boiling curves is the absence of an incipience overshoot for the CNT-coated sample. Bubble nucleation from the surface of the CNT-coated sample is observed at the initial heat flux test point, and therefore the curve follows the slope associated with the boiling regime from this lowest heat flux data point. Elimination of the incipience overshoot results in a lower substrate superheat temperature and thermal resistance over heat fluxes up to 53 W cm^{-2}, and also avoids a rapid transient temperature drop upon incipience.

Elimination of the incipience overshoot through CNT-coating of a smooth silicon surface has been previously observed for pool boiling using FC-72 [13], and is attributed to roughening of the surface and creation of vapor cavities that support vapor nucleation. While incipience overshoot has also been observed for pool boiling of FC-72 from porous copper surfaces [37] and capillary-fed boiling of water [19], this is the first demonstration of the elimination of such overshoot through CNT integration on such surfaces. The Clausius-Clapeyron equation predicts that the superheat required for vapor embryo growth and activation of boiling from a surface is inversely proportional to the cavity size for a given cavity geometry and liquid contact angle [30]. Even though this suggests that addition of nanometer-size

cavities to the micron-size cavities in a sintered powder wick alone should not decrease the required incipience superheat temperature, there are other possible ways the CNTs may act to reduce the required incipience superheat. Specifically, modification of the geometry at the exit of the microscale cavity induced by the CNT coating, such as increased wetting contact angle, cavity aspect ratio, or vapor embryo stability, may have led to the observed reduction in required activation superheat for the CNT-coated sample. These mechanisms are discussed in detail in a separate study [38] focused on quantifying the incipience superheat reduction provided by CNTs grown on 200 μm-thick sintered powder wicks.

At heat fluxes above 53 W cm^{-2}, the boiling and thermal resistance curves are nearly identical for the uncoated and coated sample (Figure 4) and the CNT-coating does not provide any performance benefit. Additionally, after a steady state was reached at 437 W cm^{-2} for the CNT-coated sample H:1, the subsequent test point caused dryout of the sample surface and testing was ceased due to a catastrophic temperature overshoot. A dramatic transient substrate temperature rise is associated with dryout, and the temperature jumps 35 °C within a 3-second temperature-recording increment. The limiting dryout heat flux thus lies between 437 and 537 W cm^{-2} based on the electrical input increment which caused dryout.

Critical heat flux (CHF) for capillary-fed boiling can be caused either by excessive vapor blanketing of the surface due to vigorous boiling (boiling limit) or by capillary starvation of the wick due to excessive pressure drop (capillary limit). Previous pool boiling studies using highly wetting dielectric fluids suggest that a CNT array grown over a boiling surface tends to increase CHF [11-14], which is contrary to the trend observed here. It is likely that the CNT coating may have reduced the capillary limit for sample H:1. Although the copper coating on the nanotubes significantly increases their hydrophilicity compared to uncoated CNTs, it may still be less wetting than the bare sintered copper powder surface, and therefore reduces the maximum sustainable capillary pressure within the wick. The extent of CHF reduction due to the CNTs was not quantified because the bare sample was not driven to CHF.

Several of the key transitional heat fluxes and regime thermal resistances are summarized in Table 1 for ease of direct quantitative comparison between the samples. In the table, R_{evap} is the average thermal resistance for a given sample over all evaporative regime heat fluxes and R_{boil} represents the average thermal resistance for heat fluxes over which the samples are observed to be in the boiling regime, i.e., from 80 to 500 W cm^{-2}. For the homogeneous samples discussed in this section, the CNT coating prevents the 4.7 °C superheat temperature overshoot by causing incipience of boiling at or below the lowest heat flux investigated. In the boiling regime the thermal resistances of the uncoated and coated samples are similar, at 0.35 and 0.37 °C/W, respectively, which is notably lower than the evaporative thermal resistance of 0.63 °C/W experienced by the uncoated sample at the lower heat flux inputs. Dryout of the CNT-coated sample above 437 W cm^{-2} is also documented in this table.

4.1.2. Homogeneous versus patterned sintered powder wicks

The results shown in Figure 5 compare the grid and wedge-patterned samples to the baseline homogeneous sintered powder wick to evaluate multi-scale porous wicks. All three samples exhibit incipience superheat temperature overshoot and the measured temperature drop upon incipience ranges from 4.1 to 4.7 °C, as shown by the boiling curves. The heat fluxes (or alternatively, superheats) at which incipience occurs for each sample are similar and lie in the range of 53 to 60 W cm^{-2} (superheats of 7.0 to 10.5 °C) as listed in Table 1. In the evaporative regime the patterned samples have a slightly higher thermal resistance than the homogeneous sample. It is noted that the high thermal resistance in the evaporative regime (compared to the boiling regime) is attributed to the added layer of conduction resistance through the wick, as explained previously. In the case of the patterned wicks, *in situ* images of the surfaces show that the patterned areas are filled with liquid in this regime. Patterning effectively replaces a large portion of water-saturated sintered copper powder area with a layer of liquid water, which increases conduction resistance through the wick. This is consistent with the evaporative thermal resistance increase due to patterning.

The performance of the patterned samples deviates from that of the homogeneous sample further following incipience of boiling. The grid-patterned sample G:0 immediately drops to a lower surface superheat than the homogeneous sample and follows a linear slope parallel to the homogeneous sample behavior, until even further diverging above 360 W cm^{-2}. This increased performance is captured as a 28.5% reduction in the average boiling resistance from 0.35 to 0.25 °C/W between the patterned and homogeneous samples. The wedge-patterned sample exhibits a more modest performance increase. The performance is the same as the homogeneous sample until 360 W cm^{-2} at which point the substrate superheat decreases. Dryout was not observed for any of the samples in Figure 5 over the range of heat fluxes tested, and hence no conclusions can be drawn about any CHF alternation caused by patterning.

Visualization confirms that patterning of sintered powder evaporators enhances capillary-fed boiling heat transfer by increasing the permeability for vapor exiting the wick, as also hypothesized in a previous investigation [22]. Figure 6 (a) shows a set of sequential images and representative sketches of boiling from the homogeneous wick at 86 W cm^{-2}. This figure and all figures containing a similar set of sequential images are extracted from video that is made available as Supplementary data provided with this paper and available online. In the images, a single bubble grows from the surface before breaking through the liquid-vapor interface and releasing vapor to the chamber. Images recorded at 15,000 fps reveal the approximate departure frequency of this nucleation site as 1500 s^{-1}. The video displays multiple other nucleation sites with bubble diameters on the order of the pore size in the background, with high departure frequencies that are not accurately resolved at 15,000 fps. Bubble departure from many individual particle pores over the heat input area is typical for boiling from the homogeneous surface.

Characteristic bubble nucleation from a grid-patterned sample is displayed in Figure 6 (b). The series of images shows that vapor preferentially agglomerates from many nucleation sites at the base of the wick and exits as a single bubble from the open grid at a lower departure frequency than in the case of the smaller bubble from a monolithic wick. While these images are shown for a relatively low heat flux test point, vapor preferentially departs the surface through these high-permeability vapor vents even at the highest heat fluxes observed. The grid-patterned sample is thus seen to provide enhancement throughout the boiling regime where vapor pressure drop through the porous layer governs performance.

The wedge-patterned sample did not exhibit such preferential vapor departure from the surface until much higher heat fluxes of 142 W cm^{-2}. Below this heat flux, bubble nucleation occurred through individual pores from the sintered powder located at the center of the wedge pattern, as it would in the homogeneous sample. Accordingly, no increase in relative performance on the boiling curve was observed for the wedge pattern until higher heat fluxes. Figure 6 (c) shows a series of images depicting preferential vapor flow out of the wedge pattern at these higher heat fluxes. The vapor bubble grows from the apex of each open wedge (closest to the center) and travels radially outward before departing from the surface. The shape of the wedge pattern, a solid sintered powder center with the widest part of the open wedge furthest from the heat input, inherently causes the effective pressure drop for vapor leaving the surface (and therefore the thermal resistance) to be larger than in the case of the grid pattern.

4.1.3. Combined CNT-coating and patterning of sintered-powder wicks

The remaining sample investigated was the CNT-coated grid-patterned sample, G:1. The boiling curve and thermal resistance curve for this sample are compared against the baseline bare homogeneous sample and the bare grid-patterned sample in Figure 7. In general, the sample retains and combines the trends observed separately for the homogeneous CNT-coated sample H:1 and the grid-patterned bare sample G:0. The CNT coating induces boiling incipience with no overshoot and hence the thermal resistance is lower than the bare samples at heat fluxes less than 65 W cm^{-2}. In the boiling regime, specifically above 187 W cm^{-2}, the grid patterning again provides increased performance compared to the bare homogeneous baseline sample due to high-permeability vapor venting from the surface. However, when compared directly against the bare grid-patterned sample in the heat flux range from 142 to 251 W cm^{-2}, the CNT-coated performance is inferior. Visualizations comparing samples G:0 and G:1 over these intermediate heat fluxes do not reveal a clear reason for the performance difference. Due to lower performance over these heat fluxes, the average boiling resistance for sample G:1 in Table 1 is not as favorable as that of sample G:0, but still yields a 14.2% reduction compared to the baseline bare homogeneous sample. Finally, dryout of the sample was observed at the maximum test heat flux of 539 W cm^{-2} (unlike the bare sample which sustained good performance at this heat flux without signs of

dryout) for the same possible reasons as discussed previously for the other CNT-coated sample tested, H:1.

While all of the individual trends due to CNT coating and microwick patterning were preserved, combining these features together did not provide any additional augmentation (such as might be expected from the creation of adequately fed and low thermal resistance CNT array evaporation/boiling regions at the base of the recessed areas). Any such performance augmentation may have been masked by the order-of-magnitude height differences between the 1 mm thick sintered powder and the ~10 μm tall CNT array. Based on imaging of the surface during testing, the CNTs were found to be entirely or partially flooded by the liquid at the base of the open grid cell over a large range of the boiling curve. Flooding of the CNT array thus prevented any gains in efficiency from thin liquid film evaporation or boiling from CNTs at the base of the grid pattern for a majority of the heat fluxes investigated.

4.1.4. Summary of vapor formation regimes

For each sample tested the high-speed imaging equipment was used to obtain video of the evaporation/boiling mechanisms at every heat flux. The vapor formation regimes identified in these visualizations are summarized in this section. Trends in the boiling curve as a function of these regimes are presented for generalized homogeneous and patterned wicks. Understanding the capillary-fed boiling heat transfer regimes for typical homogeneous and patterned sintered-powder evaporators facilitates predictive modeling of the observed characteristics. Estimation of transition between the identified regimes, as well as the performance in each regime, is crucial for design and operation of high heat flux vapor chambers.

The regimes identified for homogeneous sintered-powder wick samples are shown in Figure 8. This figure presents typical boiling and thermal resistance curves for a homogeneous sintered powder wick and the modifications caused by the addition of a CNT layer. The curves are divided into multiple regions which denote changes in thermal performance trends and observed vapor formation characteristics.

At the lowest heat fluxes, the surface remains in the evaporation regime and the resistance is governed by conduction through the wick. Addition of a CNT-coating causes transition to a localized nucleate boiling regime at lower heat fluxes than for a bare sample. The thermal resistance is reduced for the CNT-coated surface compared to the homogeneous surface over this range of heat fluxes due to presence of boiling in the wick. As the heat flux is increased, both surface morphologies transition to uniform nucleate boiling over the entire heated area, designated as regime 3 in Figure 8. Boiling incipience does not cause any observable starvation of the wick. Incipience may be a limiting condition for axially grooved heat pipes with a linear capillary flow pathx that are easily cut off by bubble formation, but the randomized pores in a sintered-powder wick provide a multitude of liquid supply paths

around the vapor that is formed. Operation in the boiling regime increases the maximum operating heat flux and reduces the surface superheat.

Further increases in heat flux cause stable recession of the liquid into the wick simultaneously with nucleate boiling (regime 4). The exact depth of free-surface recession cannot be determined from visualizations, but the liquid recedes furthest in the center-most portions of the wick region directly above the heat input area. The thermal performance is not altered by this liquid surface recession. Ultimate dryout of the wick would occur with further increases in the input heat flux. Based on the current experimental results, CHF occurs in the CNT-coated sample at lower heat fluxes than with the bare samples. High-speed visualization of the highly transient process cannot be easily captured, making it difficult to detect the mechanistic cause of dryout.

A similar regime-based description for patterned sintered-powder wicks is presented in Figure 9, and includes typical performance curves for both bare and CNT-coated types. At low heat fluxes, the recessed pattern and sintered powder remain completely saturated and evaporation occurs from the liquid-vapor interface. The schematic diagram depicting this regime shows why the thermal resistance is larger for the patterned wicks than the homogeneous wicks in the evaporation regime. Patterning replaces high-conductivity copper with water and increases the governing conduction resistance from the substrate to the evaporating menisci. Moving up along the boiling curve, the CNT-coated wick reaches the onset of nucleate boiling prior to the bare wick until they both sustain boiling in regime 3. In this regime quasi-pool boiling occurs in the patterned areas which remain completely filled with liquid. Even though vapor is generated uniformly from the base of the wick, vapor is only seen leaving through these patterned areas and no bubble departure takes place from the surrounding sintered powder. As the heat flux is further increased, liquid in the patterned recesses begins to recede. This process occurs gradually over the range of heat inputs labeled as regime 4. Recession occurs because the millimeter-size pore cannot support the increasing capillary pressure head. In this regime, nucleation still resembles pool boiling from the patterned area, the CNT layer remains completely submerged, and performance is not affected.

An increased slope in the boiling curve and further reduction in the overall thermal resistance occurs coincident with transition to regime 5. In this regime, liquid in the patterned recesses in the wick further recedes and a thin film is formed over the exposed substrate. Nucleation occurs primarily from the corners and sides of the patterned area as vapor continues to preferentially exit through the patterned openings. Bubble departure is also observed from the film itself, confirming the existence of the thin liquid layer. Figure 10 includes a series of images which show film boiling from the exposed substrate. Intense evaporation from this thin liquid film accounts for the performance increase. A similar performance increase coincident with formation of a thin liquid film has been observed for capillary-fed boiling from sintered copper screen meshes [19]. Regime 6 in Figure 9 is characterized by complete

dryout of the patterned recessed areas in the wick. Despite the occurrence of dryout in these areas, vigorous boiling from the sintered powder continues. This regime is followed by CHF and complete dryout of the wick. Practical visualization limitations prevent direct observation of the CHF mechanisms as they occur.

4.2. Survey of predictive methods

While capillary-fed boiling testing may reveal the performance characteristics and identify critical regime transitions for a given sample of interest, from an engineering design perspective it is impractical to perform similar testing and detailed visualization over a wide array of wick parameters. In order to optimize and design high heat flux vapor chambers, the regime transitions and thermal performance must be predictable across the porous wick design parameters. The available predictive methods for capillary-fed boiling are reviewed here with respect to the current testing results. In particular, the relationship between heat input and surface superheat in the evaporation and nucleate boiling regimes for homogeneous sintered powder surfaces are investigated.

In the evaporation regime the porous wick remains completely saturated with fluid and phase change occurs solely at the liquid-vapor free surface. Performance under these operating conditions is dictated by the effective thermal conductivity of the saturated porous wick which constitutes a dominant portion of the overall thermal resistance compared to the very effective evaporation heat transfer at the interface. Several models are available for estimating the effective thermal conductivity of saturated porous media based on the porosity and component thermal conductivities. Carson *et al.* [39] reviewed several models for the effective conductivity of porous materials with a single continuous phase. The Maxwell-Eucken 1 (ME1) and Maxwell-Eucken 2 (ME2) expressions given by

$$ME1: k_{eff} = k_{Cu}\frac{2k_{Cu} + k_l - 2(k_{Cu} - k_l)\varepsilon_l}{2k_{Cu} + k_l + (k_{Cu} - k_l)\varepsilon_l}, \text{ and} \tag{3}$$

$$ME2: k_{eff} = k_l\frac{2k_l + k_{cu} - 2(k_l - k_{cu})(1-\varepsilon_l)}{2k_l + k_{cu} + (k_l - k_{cu})(1-\varepsilon_l)} \tag{4}$$

represent limiting effective conductivities for the case of a continuous solid (ME1) or continuous liquid (ME2) phase. The effective medium theory (EMT) represents an intermediate bound between these two extremes which divides porous materials into internal and external porosity classifications and is given by

$$EMT: (1-\varepsilon_l)\frac{k_{cu} - k_{eff}}{k_{cu} + 2k_{eff}} + \varepsilon_l\frac{k_l - k_{eff}}{k_l + 2k_{eff}} = 0. \tag{5}$$

In a subsequent report, Wang et al. [40] proposed a co-continuous (CC) phase model. The effective conductivity for this model is given by

$$CC: (1-\varepsilon_l)\frac{(k_{cu}-k_{eff})(2k_{cu}+k_{eff})}{k_{cu}}+\varepsilon_l\frac{(k_l-k_{eff})(2k_l+k_{eff})}{k_l}=0. \quad (6)$$

The evaporation-regime surface superheat can be predicted using k_{eff} from these models and the wick thickness, δ, according to

$$\Delta T_{sl}=\frac{q''\delta}{k_{eff}}. \quad (7)$$

The predicted superheat can be compared to the experimentally measured values in the evaporation regime for the homogeneous sintered powder sample H:0. It is noted that the superheats shown earlier in Figure 4 include the substrate thermal resistance. In order to compare directly against the predicted ΔT_{sl}, the temperature drop through the substrate is estimated assuming one-dimensional heat flow and subtracted from the H:0 boiling curve temperatures, as shown in Figure 11. In the figure, lines (1-3) correspond to the superheats predicted using the ME1, EMT, and CC models for respective estimated effective conductivities of 160.5, 101.5, and 42.9 W m^{-1} K^{-1}. The ME2 result is in error by an order of magnitude and is not shown. The EMT prediction best matches the experimental results, underestimating the superheat by a mean absolute percentage error (MAPE) of 21%. This is also consistent with direct measurements of sintered copper powders which show the actual thermal conductivity to be slightly lower than EMT predictions [41]. However, it has also been observed that the measured thermal conductivity of constant-porosity sintered copper powder varies based on a host of variables such as the sintering time, temperature, and conditions which cannot be accounted for in the aforementioned conductivity models [42]. Therefore, direct wick thermal conductivity measurements are still required to accurately predict the evaporation regime superheat until more accurate sintered copper powder conductivity models are developed.

Reliable performance prediction of boiling in capillary-fed porous structures over a range of working fluids and wick materials is crucial for optimized operation of heat pipes within the boiling regime. Despite several recent studies on capillary-fed boiling from porous structures [16-20, 22-24], correlations to predict heat transfer in the boiling regime over a comprehensive range of operating conditions have not been developed. Instead, the accuracy of correlations from the more extensive field of submerged pool boiling from smooth and porous surfaces are assessed here despite the difference in the fluid-feeding mechanism. Expectedly, because they do not account for enhancement by the porous surface, established smooth surface pool boiling correlations [43-46] over-predict the surface superheat and fail to capture the boiling curve trends as shown in Figure 11. Additionally, comparison to many existing experimentally based correlations on pool boiling from porous surfaces [47,48] is difficult due to the widely differing surface geometries, surface materials, test fluids, and porous geometries used to develop the empirical correlations. However, there are instances of semi-empirical methods that predict

boiling performance for general porous media which match experimental data for multiple surfaces and fluids. Rao and Balakrishnan [49] used Darcy's law for pressure drop through the wick for a given bubble departure rate to determine the latent heat flux contribution by the Clapeyron equation. Combining these expressions with semi-empirical relations for the bubble departure rate and convective heat transfer contribution yields the equation

$$q'' = 2.4\times10^{-4}\,\frac{\rho_l\rho_g^2 \mathrm{K} h_{\mathrm{lg}}\Delta T_{sl}\left(\delta/D_p\right)^{0.8}\mathrm{Ja}^{0.22}}{\mu_g\delta T_{sat}(\rho_l-\rho_g)\varepsilon_l^{1.23}}. \tag{8}$$

This correlation is compared to the current test results in Figure 11 and shows a good match with an MAPE of 7.7%. Also, the nearly linear relationship between q'' and ΔT_{sl} better captures the trends of the curve. Smirnov [50] described boiling as evaporation heat transfer from an elementary unit cell of the porous structure represented by a fin coated with a thin liquid film. Solving for heat transfer by evaporation from this film-coated fin and fitting a single empirical constant to existing experimental data yields

$$q'' = 0.094\left(\frac{h_{\mathrm{lg}}\sigma k_l^3}{\upsilon_l}\right)^{1/6}\left(1-\varepsilon_l\right)^{1/6}k_{eff}^{1/3}\left(\frac{\Delta T_{sl}-\Delta T^*}{L_e}\right)^{5/6}. \tag{9}$$

This correlation compares extremely favorably with the current testing results and predicts the results with an MAPE of only 2.7%. The accuracy of these models in predicting the current test results also provides insight into the enhancement provided by patterning of the wick. Vapor permeability is a chief determinant of overall heat transfer performance in the models. While the models do not directly account for patterned wick surfaces, decreasing the vapor pressure drop through surface modification would assuredly result in larger heat transfer rate predictions as observed in the experimental results.

Both of these models accurately predict performance in the boiling regime for the current study; however, until they can be further verified against capillary-fed boiling from other surface geometries and fluids, their universal applicability is not assured. Also, comparisons are only made for a single particle size and porosity. It is important for design purposes that the correlations be confirmed for different wick material parameters. Finally, in order to determine when the evaporation or the boiling regime model should be used, the superheat at incipience must be known. Incipience is highly dependent on surface factors such as roughness, wettability, and oxidation which can vary slightly between samples and test runs. Therefore, a probabilistic representation of incipience versus wall superheat obtained through repeated experimentation is required to rationally draw comparisons with available incipience superheat prediction methods.

5. Conclusions

Evaporation and boiling in porous sintered powder wicks was investigated under capillary-feeding conditions as occur in high heat flux heat pipes or vapor chamber heat spreaders. Two techniques to enhance the thermal performance of wick structures – CNT-coating and micropatterning – were evaluated using a thermal facility which simultaneously records high-speed images of the wick surface and heat transfer measurements. The visualizations provide a detailed indication of the fundamental vapor-formation regimes occurring at different heat fluxes and allows correlation of the evaporation/boiling mechanisms to thermal performance trends and surface modifications. The available methods for predicting capillary-fed evaporation and boiling performance are evaluated with respect to the current dataset and yield key insights into the observed enhancement mechanisms. The main conclusions from this investigation are:

(1) Boiling incipience reduces the effective thermal resistance compared to evaporation-based operation by eliminating conduction resistance through the saturated wick and does not cause capillary starvation of the surface.

(2) CNT-coating of wicks alters the surface nucleation cavities and reduces the required superheat for incipience, thus reducing overall thermal resistance at low heat fluxes.

(3) Patterning of wicks to introduce high-permeability paths into the wick structure reduces thermal resistance in the boiling regime by increasing the permeability of the wick to exiting vapor and by forming an evaporating thin liquid film at the base of the patterned area at high heat fluxes.

(4) Performance within the observed evaporation regime can be predicted assuming conduction through the saturated porous layer; however, generalized models for the wick effective thermal conductivity are inadequate for sintered copper powders.

(5) Comparisons to semi-empirical correlations for boiling from porous media are encouraging and corroborate evidence that vapor permeability exiting the wick is a key factor in boiling performance.

Acknowledgements

This material is based upon work supported by the Defense Advanced Research Projects Agency (DARPA) and Space and Naval Warfare Systems Center (SPAWAR/SYSCEN) San Diego, CA under Contract No. N66001-08-C-2011. The authors thank Mark T. North of Thermacore, Inc., for fabrication and supply of the sintered copper powder samples and Professor Timothy S. Fisher of Purdue University for contributing to this work with the carbon nanotube synthesis.

References

[1] U. Vadakkan, J.Y. Murthy, S.V. Garimella, Transient analysis of flat heat pipes, in: Proceedings of HT2003 ASME Summer Heat Transfer Conference, Las Vegas, Nevada, 2003.

[2] J.A. Weibel, S.V. Garimella, J.Y. Murthy, D.H. Altman, Design of integrated nanostructured wicks for high-performance vapor chambers, IEEE Transactions on Components, Packaging, and Manufacturing Technology, 1 (6) (2011) 859-867.

[3] J.A. Weibel, S.S. Kim, T.S. Fisher, S.V. Garimella, Carbon nanotube coatings for enhanced capillary-fed boiling from porous microstructures, Nanoscale and Microscale Thermophysical Engineering, *Paper in Print*.

[4] M.A. Hanlon, H.B. Ma, Evaporation heat transfer in sintered porous media, Journal of Heat Transfer, 125 (4) (2003) 644-652.

[5] T.W. Davis, S.V. Garimella, Thermal resistance measurement across a wick structure using a novel thermosyphon test chamber, Exp. Heat Transfer 21 (2) (2008) 143–154.

[6] J.A. Weibel, S.V. Garimella, M.T. North, Characterization of evaporation and boiling from sintered powder wicks fed by capillary action, International Journal of Heat and Mass Transfer, 53 (19-20) (2010) 4204-4215.

[7] C. Li, G.P. Peterson, Y. Wang, Evaporation/boiling in thin capillary wicks (I) – wick thickness effects, Journal of Heat Transfer 128 (12) (2006) 1312–1319.

[8] C. Li, G.P. Peterson, Evaporation/boiling in thin capillary wicks (II) – effects of volumetric porosity and mesh size, Journal of Heat Transfer 128 (12) (2006) 1320–1328.

[9] C. Li, G.P. Peterson, J. Li, N. Koratkar, The visualization of thin-film evaporation on thin micro sintered copper mesh screen, in: Proceedings of the ASME Summer Heat Transfer Conference, Jacksonville, FL, 2008, pp. 645–650.

[10] Y. Zhao, C.I. Chen, An investigation of evaporation heat transfer in sintered copper wicks with microgrooves, in: Proceedings of 2006 ASME International Mechanical Engineering Congress and Exposition, Chicago, IL, 2006.

[11] T. Semenic, I. Catton, Experimental study of biporous wicks for high heat flux applications, International Journal of Heat and Mass Transfer 52 (21–22) (2009) 5113–5121.

[12] E.G. Merilo, Experimental investigation of boiling heat transfer in bidispersed porous media, Master's Thesis, University of California, Los Angeles, CA, 2002.

[13] J.J. Zhou, F. Noca, M. Gharib, Flow conveying and diagnosis with carbon nanotube arrays, Nanotechnology, 17 (19) (2006) 4845-4853.

[14] R. Ranjan, S.V. Garimella, J.Y. Murthy, K. Yazawa, Assessment of nanostructured capillary wicks for passive, two-phase heat transport, Nanoscale and Microscale Thermophysical Engineering, 15 (3) (2011) 179-194.
[16] L. Feng, S. Li, Y. Li, H. Li, L. Zhang, J. Zhai, Y. Song, B. Liu, L. Jiang, D. Zhu, Super-hydrophobic surfaces: from natural to artificial, Advanced Materials, 14 (24) (2002) 1857-1860.
[17] F. Wang, S. Arai, M. Endo, Metallization of multi-walled carbon nanotubes with copper by an electroless deposition process, Electrochemisty Communications, 6 (10) (2004) 1042-1044.
[18] Y. Peng, Q. Chen, The synthesis of a copper/multi-walled carbon nanotube hybrid nanowire in a microfluidic reactor, Nanotechnology, 20 (23) (2009).
[19] G.A. Powell, Controlled synthesis of CNT-based nanostructures for enhanced boiling and wicking, Master's Thesis, Purdue University, West Lafayette, IN, 2009.
[20] H.S. Ahn, N. Sinha, M. Zhang, D. Banerjee, S. Fang, R.H. Baughman, Pool boiling experiments on multiwalled carbon nanotube (MWCNT) forests, Journal of Heat Transfer, 128 (12) (2006) 1335-1342.
[21] V. Sathyamurthi, H.S. Ahn, D. Banerjee, S.C. Lau, Subcooled pool boiling experiments on horizontal heaters coated with carbon nanotubes, Journal of Heat Transfer, 131 (7) (2009) 071501-1-071501-10.
[22] S. Ujereh, T. Fisher, I. Mudawar, Effects of carbon nanotube arrays on nucleate pool boiling, International Journal of Heat and Mass Transfer, 50 (19-20) (2007) 4023-4038.
[23] S. Launay, A.G. Fedorov, Y. Joshi, A. Cao, P.M. Ajayan, Hybrid micro-nano structured thermal interfaces for pool boiling heat transfer enhancement, Microelectronics Journal, 37 (11) (2006) 1158-1164.
[30] M. Hashimoto, H. Kasai, K. Usami, H. Ryoson, K. Yazawa, J.A. Weibel, S.V. Garimella, Nano-structured two-phase heat spreader for cooling ultra-high heat flux sources, in: Proceedings of the 14th International Heat Transfer Conference, Washington, D.C., 2010.
[31] Q. Cai, C-L. Chen, Design and test of carbon nanotube biwick structure for high-heat-flux phase change heat transfer, Journal of Heat Transfer 132 (5) (2010) 052403-1-052403-8.
[36] S.S. Kim, J.A. Weibel, T.S. Fisher, S.V. Garimella, Characterization of capillary-fed carbon nanotube vapor chamber wicks, Journal of Heat Transfer, *In Review*.
[37] K.N. Rainey, S.M. You, S. Lee, Effects of pressure, subcooling, and dissolved gas on pool boiling heat transfer from microporous surfaces in FC-72, Journal of Heat Transfer 125 (1) (2003) 75-83.
[38] J.A. Weibel, A.S. Kousalya, T.S. Fisher, S.V. Garimella, Characterization and nanostructured enhancement of boiling incipience in capillary-fed, ultra-thin sintered powder wicks, in: The 13th

Intersociety Conference on Thermal and Thermomechanical Phenomenon in Electronic System, San Diego, CA, 2012 (in review).
[39] J.K. Carson, S.J. Lovatt, D.J. Tanner, A.C. Cleland, Thermal conductivity bounds for isotropic, porous materials, International Journal of Heat and Mass Transfer 48 (11) (2005) 2150–2158.
[40] J. Wang, J.K. Carson, M.F. North, D.J. Cleland, A new structural model of effective thermal conductivity for heterogeneous materials with co-continuous phases, International Journal of Heat and Mass Transfer 51 (9-10) (2008) 2389-2397.
[41] Y. Lin, T. Semenic, I. Catton, Thermophysical properties of monoporous sintered copper, in: Proceedings of the ASME Summer Heat Transfer Conference, San Francisco, CA, 2005, pp. 17–23.
[42] K.K. Bodla, J.Y. Murthy, S.V. Garimella, Direct simulation of thermal transport through sintered wick microstructures, Journal of Heat Transfer 134 (1) (2012) 012602 (1-10).
[43] W.M. Rohsenow, Method of correlating heat-transfer data for surface boiling of liquids, American Society of Mechanical Engineers – Transactions 74 (6) (1952) 969-975.
[44] I.L. Mostinski, Application of the rule of corresponding states for calculation of heat transfer and critical heat flux, Teploenergetika 4 (1963) 66.
[45] M.G. Cooper, Saturation nucleate pool boiling; a simple correlation, In: 1st UK National Conference on Heat Transfer, Leeds, England, 1984, pp. 785-793.
[46] D. Gorenflo, Pool boiling, VDI-Verlag GmbH, Dusseldorf, 1993.
[47] A. Brautsch, P.A. Kew, The effect of surface conditions on boiling heat transfer from mesh wicks, In: Proceedings of the 12th International Heat Transfer Conference, Grenoble, 2002.
[48] K. Nishikawa, T. Ito, K. Tanaka, Enhanced heat transfer by nucleate boiling on a sintered metal layer, Heat Transfer – Japanese Research 8 (2) (1979) 65-81.
[49] S.M. Rao, A.R. Balakrishnan, Analysis of pool boiling heat transfer over porous surfaces, Heat and Mass Transfer 32 (6) (1997) 463-469.
[50] G.F. Smirnov, Approximate theory of heat transfer with boiling on surfaces covered with capillary-porous structures, Thermal Engineering (Teploenergetika) 24 (9) (1977) 55-58.

List of Tables

List of Figures

to equations 8 and 9. The correlations are evaluated using saturated fluid properties at 100 °C and the following wick parameters when applicable: D = 100 μm, k_{Cu} = 400 W m^{-2}K^{-1}, δ = 1 mm, ε = 0.5.

Table 1. Summary of the thermal characterization test results.

Sample ID	Microwick Geometry	Coating	Incipience q'' (W/cm^2)	Incipience ΔT (°C)	Incipience ΔT_{drop} (°C)	q''_{evap} (Wcm^{-2})	R_{evap} (C/W)	q''_{boil} (Wcm^{-2})	R_{boil} (C/W)	Dryout (Wcm^{-2})
H:0	homogeneous	bare	53-70	9.6	4.7	25-53	0.63	70-514	0.349	N/A
G:0	grid pattern		45-60	7.0	4.1	26-43	0.69	60-558	0.253	N/A
W:0	wedge pattern		52-68	10.5	4.6	22-52	0.77	68-553	0.340	N/A
H:1	homogeneous	CNT-coated	0-30	N/A	N/A	N/A	N/A	36-437	0.369	>437
G:1	grid pattern		0-31	N/A	N/A	N/A	N/A	31-539	0.299	>539

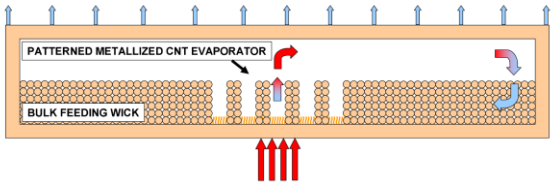

Figure 1. Schematic cross-section of a vapor chamber utilizing an evaporator section composed of metallized CNTs grown over patterned sintered copper powder.

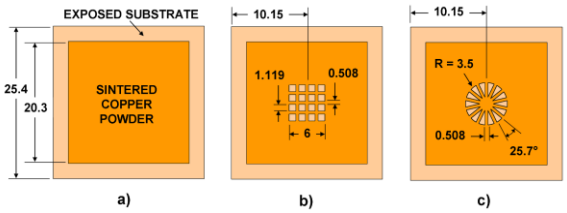

Figure 2. Dimensions of the (a) homogeneous, (b) grid-patterned, and (c) wedge-patterned sintered copper powder microwick layers. All dimensions are shown in mm.

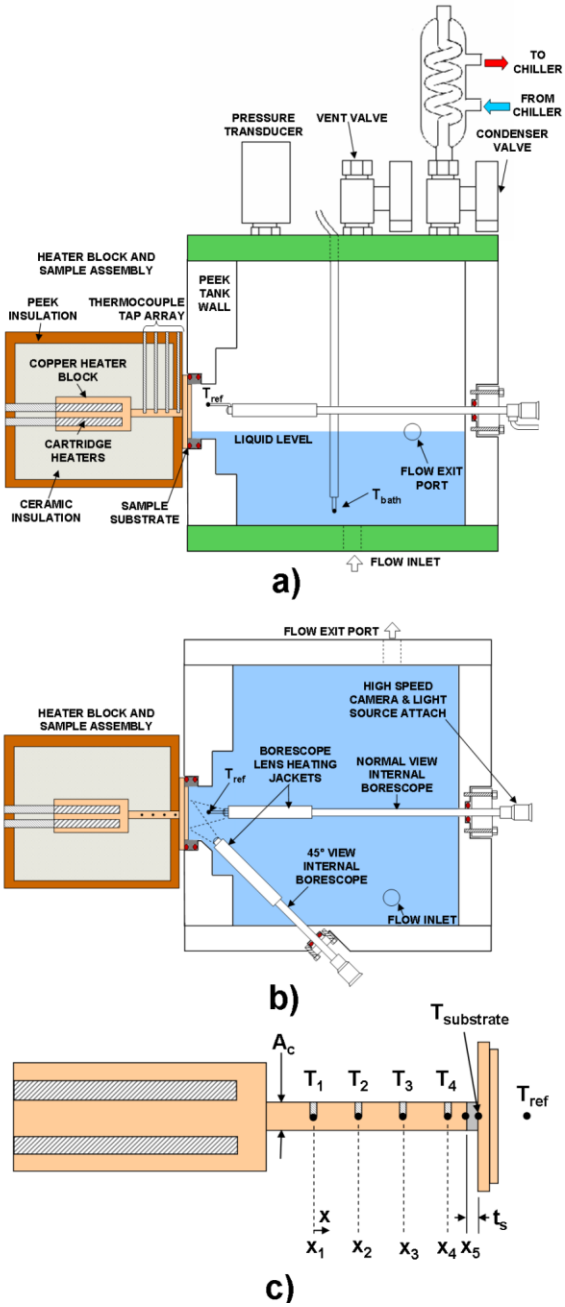

Figure 3. (a) Side-view and (b) plan-view cross sections of the capillary-fed boiling experimental facility test chamber, and (c) detailed illustration of the copper heater block temperature measurements used to determine the input heat flux and substrate temperature.

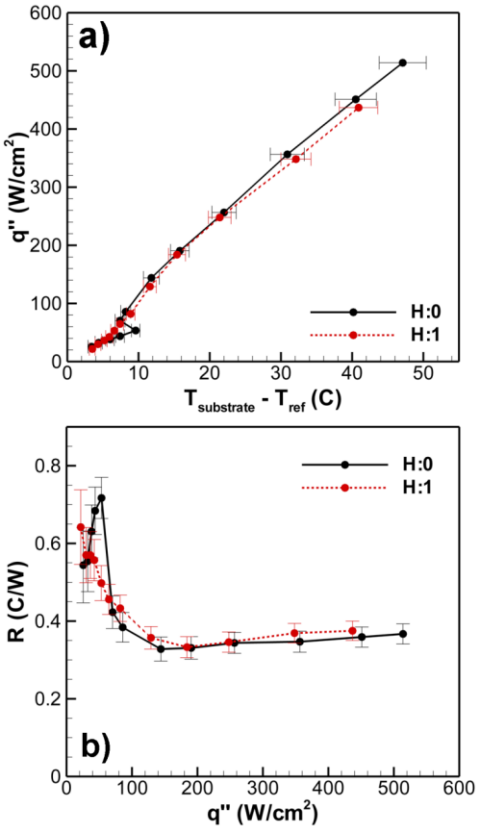

Figure 4. Comparison of the baseline homogeneous sintered powder sample H:0, against a CNT-coated homogeneous sample H:1 with a (a) boiling curve, and (b) thermal resistance as a function of input heat flux. Input heat flux uncertainty bars are not shown but are universally less than ±5%.

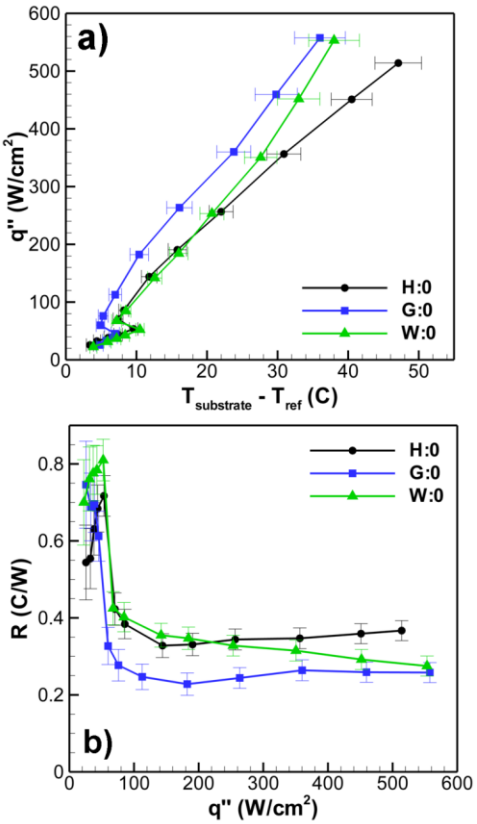

Figure 5. Comparison of homogeneous (H:0), grid-patterned (G:0), and wedge-patterned (W:0) sintered-powder samples with a (a) boiling curve, and (b) thermal resistance as a function of input heat flux. Input heat flux uncertainty bars are not shown but are universally less than ±5%.

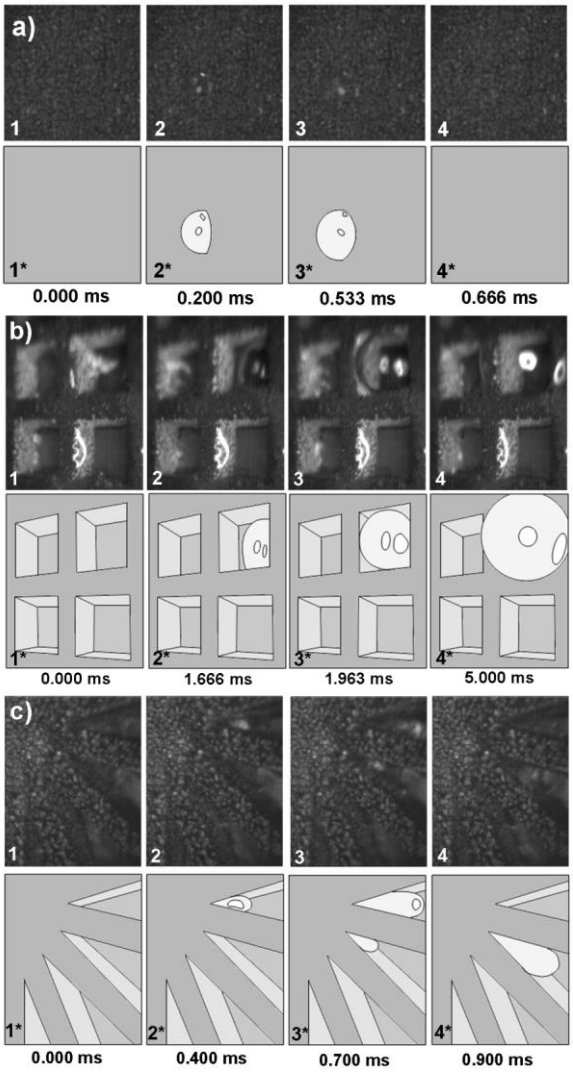

Figure 6. Series of images and diagrammatic representations of bubble nucleation from the (a) homogeneous sintered powder wick H:0 at 86 W cm^{-2} at 15,000 fps, (b) grid-patterned sintered powder wick G:1 at 31 W cm^{-2} at 6,000 fps, and (c) wedge-patterned sintered powder wick W:0 at 142 W cm^{-2} at 10,000 fps. The images are extracted from videos provided as supplementary data.

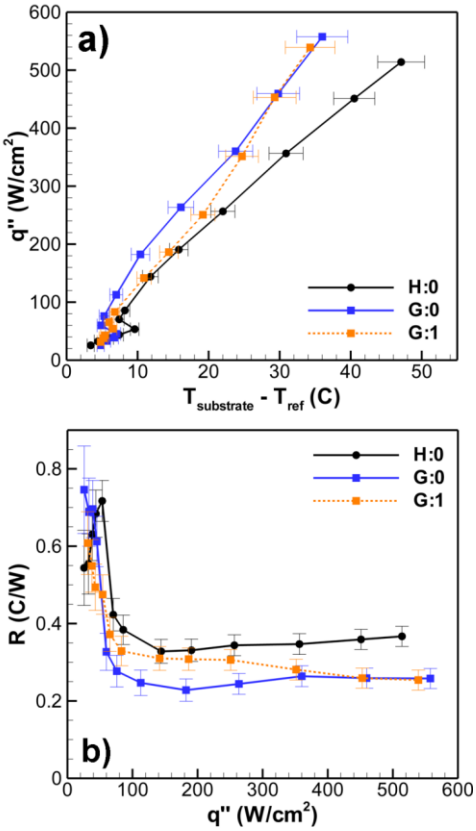

Figure 7. Comparison of grid-patterned sintered powder sample G:0, against CNT-coated grid-patterned sample G:1, with a (a) boiling curve, and (b) thermal resistance as a function of input heat flux. The baseline homogeneous sintered-powder sample H:0 is also shown. Input heat flux uncertainty bars are not shown but are universally less than ±5%.

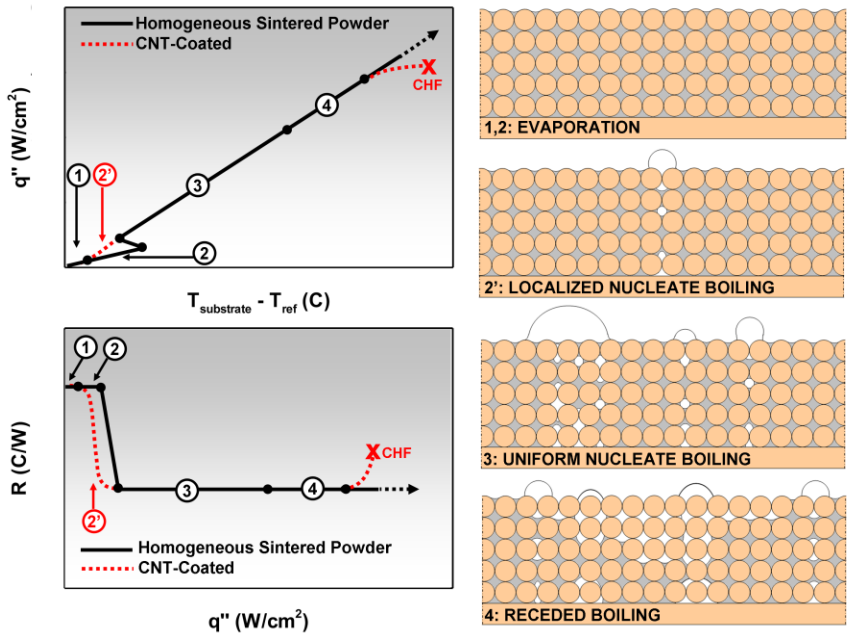

Figure 8. Schematic diagram of typical vapor formation regimes along the boiling curve for homogeneous sintered powder wicks. Expected modifications to the curve and regimes induced by CNT-coating are shown as dashed lines.

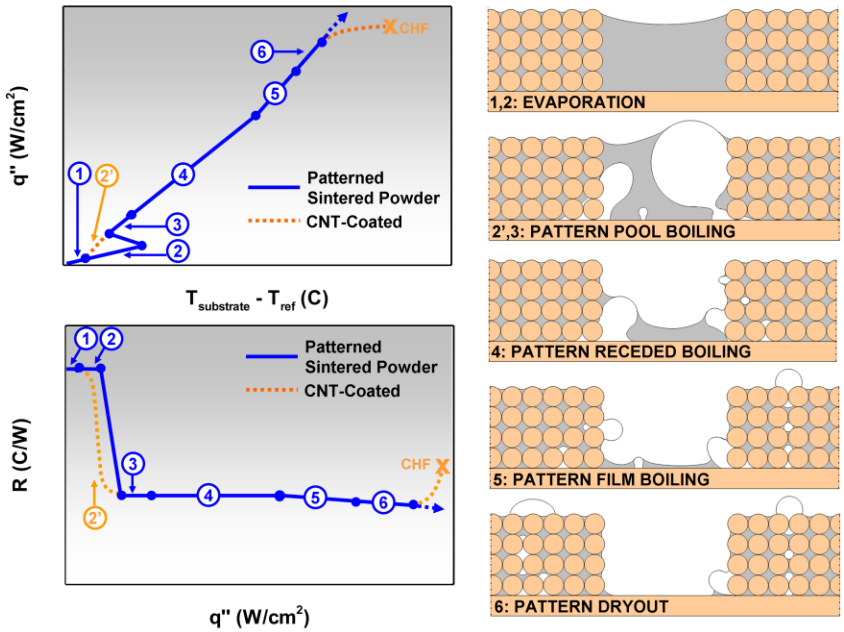

Figure 9. Schematic diagram of typical vapor formation regimes along the boiling curve for patterned sintered powder wicks. Expected modifications to the curve and regimes induced by CNT-coating are shown as dashed lines.

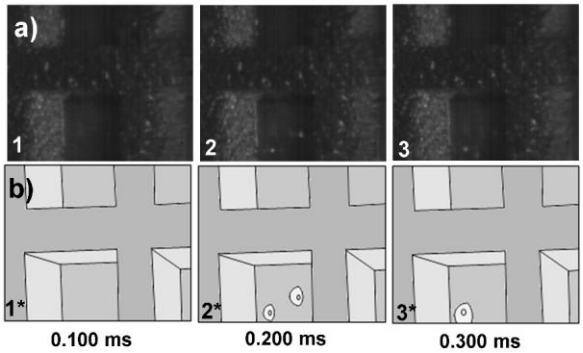

Figure 10. Series of (a) images and (b) diagrammatic representations of film boiling from the grid-patterned sintered powder wick G:1 at 352 W cm^{-2}. The images are extracted from video recorded at 10,000 fps (video is provided as Supplementary data).

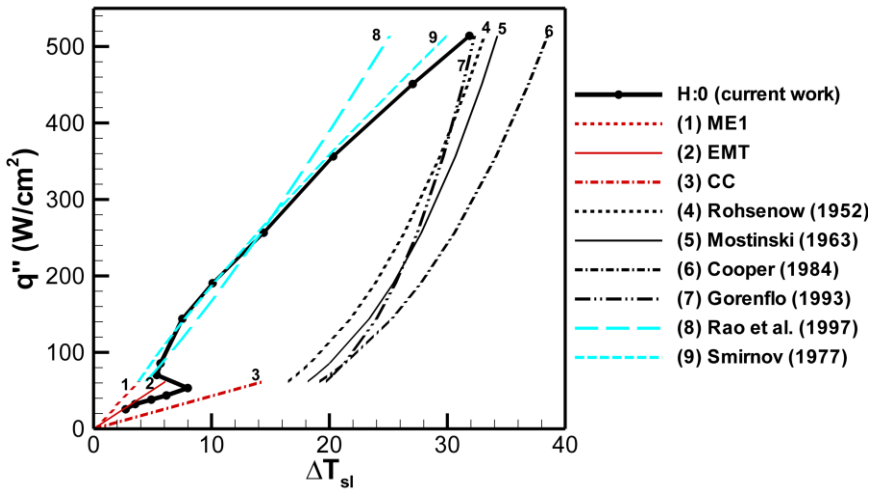

Figure 11. Comparison of results from prediction methods with the present experimental measurements in the form of a boiling curve for sample H:0. The evaporation regime is compared to wick thermal conductivity predictions (red lines 1-3) according to equations 3, 5, and 6. The boiling regime is compared to classical pool boiling correlations (black lines 4-7) according to [35-38] and porous surface boiling correlations (blue lines 8-9) according to equations 8 and 9. The correlations are evaluated using saturated fluid properties at 100 °C and the following wick parameters when applicable: D = 100 μm, k_{Cu} = 400 W m^{-2}K^{-1}, δ = 1 mm, ε = 0.5.